Real-space manifestation of ferroic multipoles in altermagnetic MnF_2

Iurii Kibalin,[1] Dalila Bounoua,[2] José A. Rodriguez Velamazán,[3] Oscar Fabelo,[3] Navid Qureshi,[3] Quentin Faure,[2] Philippe Bourges,[2] Victor Balédent,[4,2] Jian-Rui Soh,[5,6] Jeffrey Rau,[7] Paul McClarty,[2] and Arsen Gukasov[2]

[1]*Data Management and Scientific Computing, European Spallation Source, ERIC, 2800 Kongens Lyngby, Denmark*

[2]*Laboratoire Léon Brillouin, CEA, CNRS, CEA-Saclay, 91191 Gif-sur-Yvette, France*

[3]*Institut Laue-Langevin, 71 avenue des Martyrs, 38042 Grenoble, France*

[4]*Laboratoire de Physique des Solides, CNRS, Université Paris-Saclay, 91405 Orsay, France*

[5]*Quantum Innovation Centre (Q.InC), (A*STAR), 138634, Singapore*

[6]*Centre for Quantum Technologies, National University of Singapore, 117543, Singapore*

[7]*Department of Physics, University of Windsor, Windsor, Ontario N9B 3P4, Canada*

Abstract

Altermagnets are unconventional spin split magnets arising from the zero spin-orbit coupled limit. They host a magnetic multipolar order parameter yet direct real-space observation of these multipoles has remained elusive. Here we use polarized-neutron diffraction to reconstruct the three-dimensional magnetization density of the prototypical altermagnet MnF_2. By exploiting symmetry-selective magnetic reflections, we separate the dominant spherical Mn^{2+} contribution from the much weaker anisotropic Mn magnetization and the covalent spin polarization of the fluorine ligands. The reconstructed spin density reveals a finite fluorine ion moment together with an anisotropic Mn magnetization consistent with the symmetry-allowed altermagnetic rank-5 magnetic multipole O_{52}(magnetic triacontadipole). These results provide direct real-space evidence of ferroic multipolar order in an altermagnet and establish polarized-neutron diffraction as a powerful probe of hidden magnetic multipoles in quantum materials.

I. INTRODUCTION

Altermagnets are a class of compensated collinear magnets with spin-split electronic bands allowed by their special magneto-crystalline symmetries [1–5]. Unlike simple antiferromagnets, the magnetic sublattices of altermagnets are connected by lattice rotation or mirror operations. In the zero spin-orbit coupling limit where altermagnetism is most cleanly defined, the electronic bands have the spin projection as a good quantum number and magnons have a well-defined chirality and both exhibit a spin reversal under the same point group operation that swaps the magnetic sublattices [1–3, 5]. The nature of the anisotropic momentum space spin-splitting lends itself to a natural classification into d-wave, g-wave and i-wave systems. The magnetic anisotropy of altermagnets combined with magnetic compensation are very attractive for potential spintronics applications in real materials as spin-orbit coupling may only weakly perturb the principal zero spin-orbit coupling effect [6].

To date, several altermagnetic materials have been characterized as such via transport measurements and spectroscopy [7] for example in the now canonical examples MnTe [8–12] and CrSb [13–17]. Here we focus on the magnetic insulator MnF_2. Altermagnetism in this material has been characterized through direct visualization of the opposed spin polarizations of the magnonic bands using polarized inelastic neutron scattering [18].

The magnetic anisotropy of altermagnets in momentum space is the momentum space

realization of some distinctive local order parameter. While the staggered magnetization is a common order parameter in all altermagnets, it typically has the feature that the magnetic sublattice *considered alone* has a higher non-altermagnetic symmetry than that of the full magneto-crystalline structure. Therefore, any local order parameter respecting the altermagnetic symmetries must be some kind of multipole [2, 3, 19–22]. In practice, one may construct such multipoles directly from clusters of several atomic sites [3, 19]. However, first principles calculations on MnF_2 revealed a distinctively altermagnetic multipolar contribution in the form of specific ferroic multipoles in the local magnetization density [20]. Such ferroic multipoles generalize to all altermagnets inherited from the pristine zero spin-orbit coupled limit [21–23]. While all altermagnetic properties could be viewed as being tied to such multipolar order on symmetry grounds, it is of interest to image the multipoles directly.

Building on earlier work on MnF_2 [24, 25] in this work, we employ polarized neutron diffraction (PND) to reconstruct the full three-dimensional magnetization density of MnF_2 in real space. This technique is uniquely suited to probing very subtle magnetic features, revealing both the radial extent of the unpaired electrons and deviations from spherical symmetry, as well as covalent spin density transferred to ligand atoms. Using high performance PND diffractometer D3 at the ILL and newly developed software based on magnetic space-group theory, maximum entropy method (MEM) and multipole analysis [26], we quantitatively determine the covalent spin density on the fluorine ligands. We further analyze the anisotropy of the Mn spin density, giving evidence for the altermagnetic multipolar order in this compound.

Although polarized neutron diffraction has proven highly effective for ferro- and ferrimagnets, it has rarely been applied to compensated magnets [27]. In these latter systems, a measurable polarization dependence arises only under the conditions that magnetic atoms carrying opposite spins must be related by a symmetry element of the space group other than a lattice translation or inversion symmetry [22, 28, 29]. These are precisely the necessary conditions for altermagnetism making them excellent candidate materials for further investigation using polarized neutrons.

We organize the paper as follows. In the following section (Section III), we briefly introduce the polarized neutron diffraction technique and some of the specifics of the MnF_2 experiment. Section III A introduces the symmetry-allowed multipoles in MnF_2. We then present results of the diffraction experiment. On the basis of these results we show (Section III B)

that, in addition to spontaneous moments being present on the magnetic manganese ions, the fluorine moments in MnF_2 are also magnetically ordered in such a way that reflects the underlying altermagnetic symmetries. We point out that the fluorine moments make a contribution to a magnetic multipolar order parameter connected to the altermagnetism. Then, in Section III C we show results of a maximum entropy fit to obtain the microscopic magnetization density within the unit cell. This then provides (Section III D) evidence for the presence of asphericities of the magnetization density around the manganese ions that contribute to altermagnetic multipolar order parameters. We comment on plausible implications of these magnetization densities for the altermagnetic exchange pathways in the supplementary material IV.

II. METHODS

Polarized neutron diffraction was carried out on a high quality single crystal of MnF_2 on the D3 spectrometer at the ILL facility. The measured scattering intensity has three contributions of interest $I^{\pm} = I_{\rm n} + I_{\rm m} \pm I_{\rm nm}$ the first term originating from the nuclear structure and the second from the magnetic structure. These two terms are time reversal even. The third term is the nuclear-magnetic interference term. Unlike the first two terms, it depends on the incident neutron polarization reversing sign when the polarization is flipped or when the intrinsic moments are reversed. For the experimental refinement it is useful to introduce the flipping ratio $R = I^+/I^-$ and asymmetry parameter $As = (I^+ - I^-)/(I^+ + I^-) = 2I_{\rm nm}/(I_{\rm n} + I_{\rm m})$ − the latter providing direct insight into the polarization dependent interference term relative to the remaining contributions to the intensity.

In MnF_2, it is useful to separate out contributions from the *even* ($h+k+l = 2n$) and *odd* reflections ($h+k+l = 2n+1$). For the nuclear structure on its own, the manganese sublattice contributes only to the even reflections while fluorine nuclei contribute to both. Turning to the magnetic signal, the simple antiferromagnetic structure on the Mn sites (the spherical Mn contribution) is the dominant contribution and appears only in the odd reflections but in both $I_{\rm m}$ and $I_{\rm nm}$. The magnetic contribution to the even peaks belongs to any covalency on the fluorine sites and any asphericity on the manganese sites. Therefore the even peaks are of particular interest in connection to altermagnetism.

The magnetic structure of MnF_2 supports two 180° antiferromagnetic domains, distin-

guished by the sign of the Néel vector $\mathbf{N}$, and denoted $\mathbf{N}_{\pm}$. In order to make use of the neutron polarization it was necessary to achieve a majority single-domain state. Field-cooling at 1 T yielded a nearly single-domain state (98% $\mathbf{N}_{-}$), with the Néel vector antiparallel to the applied field. A separate field cooling experiment down to 6 T inverted the domain population relative to the first experiment, yielding approximately 86% of the $\mathbf{N}_{+}$ domain consistent with earlier observations [30]. For further details of the domain selection see the supplementary section.

III. RESULTS AND DISCUSSION

A. Characterization of altermagnets through multipolar order

Altermagnets are collinear compensated magnets with a net staggered magnetization $\mathbf{N} = \mathbf{M}_A - \mathbf{M}_B$ where $\mathbf{M}_I$ is the magnetization on sublattice $I = A, B$. Taking into account the full magneto-crystalline symmetries and assuming that the magnetic order does not break lattice translation symmetry, altermagnetism is characterized by $\mathbf{N}$ transforming as a 1D non-trivial irreducible representation of the point group of the lattice. Looking for order parameters at zero spin-orbit coupling with identical transformation properties one finds in all altermagnets a multipolar order parameter of the form

$$\mathbf{O}_{m_1 \dots m_p} = \int d^3\mathbf{r}[r_{m_1} \dots r_{m_p}]\mathbf{m}(\mathbf{r}) \tag{1}$$

where $[\dots]$ is a real space multipole and $\mathbf{m}(\mathbf{r})$ is the rotationally symmetric local magnetization density. As this transforms like the Néel order parameter (once all nonmagnetic sites are included) [21], cooling through T_N also leads to a nonzero expectation value for this multipole.

In other words, each local moment is associated with some generally aspherical local magnetization density that can be expanded in time odd multipoles. Among allowed multipoles, there is one ferroic multipole (preserving sign from one magnetic sublattice to another), to leading order, whose intrinsic transformation properties directly capture the magneto-crystalline symmetries.

For example, MnF_2, (characterized by magnetic space group $P4'_2/\mathrm{mnm}'$) contains two magnetic sublattices with equal and opposite moments related by a four-fold rotation around the axis of the moment, time reversal and $\frac{1}{2}\frac{1}{2}\frac{1}{2}$ translation. In the presence of magnetic

anisotropies that pin the local moments along the c axis the Landau theory leads to an xym_z multipole to leading order in the multipole expansion [20] descended from the $xy\mathbf{m}$ multipole coming from the spin-orbit free limit. This multipole respects the altermagnetic symmetries. Combining the real space and magnetic components gives a single magnetic multipole with O_{32-} character. This notation for the multipoles generalizes to O_{lm}. For this instance, $l = 3$ means that the object is an octupole while $m = 2$ specifies the components $(x \pm iy)^2 m_z$. The multipole is time reversal odd and is therefore magnetic. Later in this work, we shall see that a symmetry-allowed multipole of higher order $-$ xyz^2m_z $-$ is important in MnF_2. The existence of this multipole, O_{52}, like that of its lower order counterpart O_{32}, captures altermagnetic symmetries in a local order parameter. Below we discuss other symmetry-allowed multipoles in MnF_2.

B. Polarized neutron diffraction

An initial refinement of the flipping ratios R was performed within the CRYSPY software [26] on the 1 T dataset assuming that the magnetization resides solely on the Mn sites and follows the spherical Mn^{2+} free-ion form factor [31]. The *odd* reflections exhibit very large flipping ratios and are therefore sensitive to extinction and multiple scattering. These effects were minimized by using a thin plate-shaped sample and by applying extinction corrections. Extinction corrections have a negligible effect on the even reflections. This model yielded a Mn moment of $m_{\mathrm{Mn}} = -5.18(4)\,\mu_B$ but produced a poor agreement factor ($\chi^2 = 63.4$), with the largest discrepancies occurring for the *even* reflections. These reflections are particularly sensitive to magnetization on the fluorine sites, indicating that a purely Mn-centered model is insufficient as concluded in Refs. [24, 25, 30].

Introducing a collinear moment on the fluorine atoms can be done without breaking the $P4_{2'}/\mathrm{mnm}'$ magnetic symmetry. The symmetry fixes the fluorine moments to the pattern characteristic of altermagnetic ordering: the four-fold screw axis reverses the ligand moment and the inversion symmetry fixes the moments of other two fluorine sites. Allowing for a finite fluorine moment dramatically improved the refinement, reducing the agreement factor to $\chi^2 = 5.58$ and yielding

$$m_{\mathrm{Mn}} = -5.18(2)\,\mu_B, \qquad m_{\mathrm{F}} = 0.028(1)\,\mu_B. \tag{2}$$

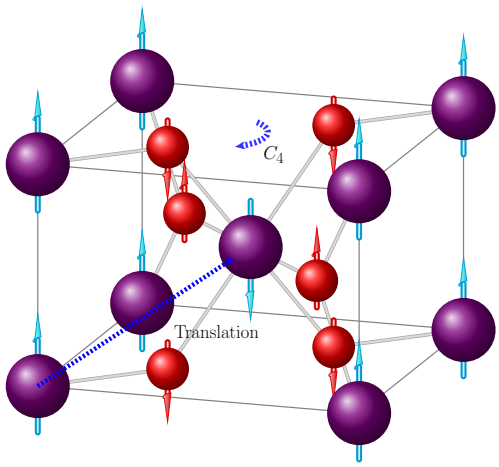

FIG. 1. **Magnetic structure of MnF_2.** Antiferromagnetic arrangement of Mn moments at 1 T, including the small but finite ligand spin polarization on the fluorine sites. The four-fold screw axis reverses the ligand moment, a hallmark of altermagnetic symmetry. The moments on the fluorine ions have been multiplied by a factor 100 to make them more clearly visible.

This refinement reveals a small but clearly resolved fluorine moment antiparallel to the nearest neighbor Mn moment giving quantitative confirmation of the result in Ref. [24] and also supported by recent first principles calculations [4]. The refined magnetic structure for the $\mathbf{N}_-$ domain at 1 T is shown in Fig. 1. This result for the fluorine moment is consistent with the bound given in Refs. [24, 25].

The 6 T dataset was analyzed in the same manner, with the domain population included as a refinement parameter. The refinement confirmed that after crossing the spin-flop transition the domain balance was inverted, with 86(2)% of the sample in the $\mathbf{N}_+$ domain. Neglecting the fluorine moment again led to a poor fit ($\chi^2 = 34.5$), whereas including it produced an excellent agreement:

$$m_{\mathrm{Mn}} = 5.14(2)\,\mu_B, \qquad m_{\mathrm{F}} = -0.028(2)\,\mu_B, \tag{3}$$

with $\chi^2 = 4.17$ and the expected sign reversal.

The inversion of the fluorine moment under the four-fold screw axis is a direct manifestation of altermagnetic symmetry. Moreover, the ensemble of the four fluorine magnetic moments in the unit cell forming an octahedron around Mn ion can be viewed as a cluster

($\mathbf{k} = 0$) magnetic octupole [32, 33] expressed as

$$O_{32}(\mathbf{k} = 0) = \sum_{i=1}^{4} x_{\mathrm{i,F}}\, y_{\mathrm{i,F}}\, m_{\mathrm{i,F}}. \tag{4}$$

Such octupolar order is expected to induce an asphericity of the Mn spin density, which in turn may contribute to the odd magnetic reflections. To quantify the Mn spin-density asphericity, a more powerful approach is required; we therefore turn to a maximum-entropy-method (MEM) reconstruction. For further details see the supplementary material.

C. Maximum Entropy Method

For collinear magnetic structures with real nuclear structure factors F_N, the solution of equation for flipping ratios given in Method section yields the magnetic structure factors $M(\mathbf{k})$, which are the Fourier coefficients of the longitudinal magnetization density in the unit cell,

$$M(\mathbf{k}) = \int_{\mathrm{cell}} m(\mathbf{r})\, e^{i\mathbf{k}\cdot\mathbf{r}}\, d^3\mathbf{r}. \tag{5}$$

A classical Fourier inversion of these coefficients, or a more sophisticated reconstruction using the Maximum Entropy Method (MEM), provides direct real-space information on the magnetization density. MEM is known to yield substantially cleaner real-space densities than conventional Fourier syntheses by suppressing noise and truncation artifacts.

For this work, we developed a MEM procedure adapted to antiferromagnets. It is similar in spirit to the two-channel approach developed in Ref. [34], but incorporates the full magnetic space group and allows constrained magnetic moments in the asymmetric unit [35]. The refined Mn and F moments, $\mu_{\mathrm{Mn}} = -5.18\,\mu_B$ and $\mu_{\mathrm{F}} = 0.028\,\mu_B$, were assigned to two independent positive density channels, respectively.

To test for asphericity in the Mn spin density, the MEM reconstruction was performed using a deliberately unfavorable, non-uniform prior [34]. This prior consists of spherically symmetric magnetization densities centered on the Mn and F sites, constructed analytically from the refined moments and the radial integrals obtained in the least-squares refinement. Because this prior is strongly biased toward spherical densities, any asphericity emerging in the MEM solution must be supported by the experimental data.

Figure 2a,b show the reconstructed three-dimensional spin density for the 1 T dataset at 2 K. Despite the spherical prior, the reconstruction robustly reveals two features: a finite

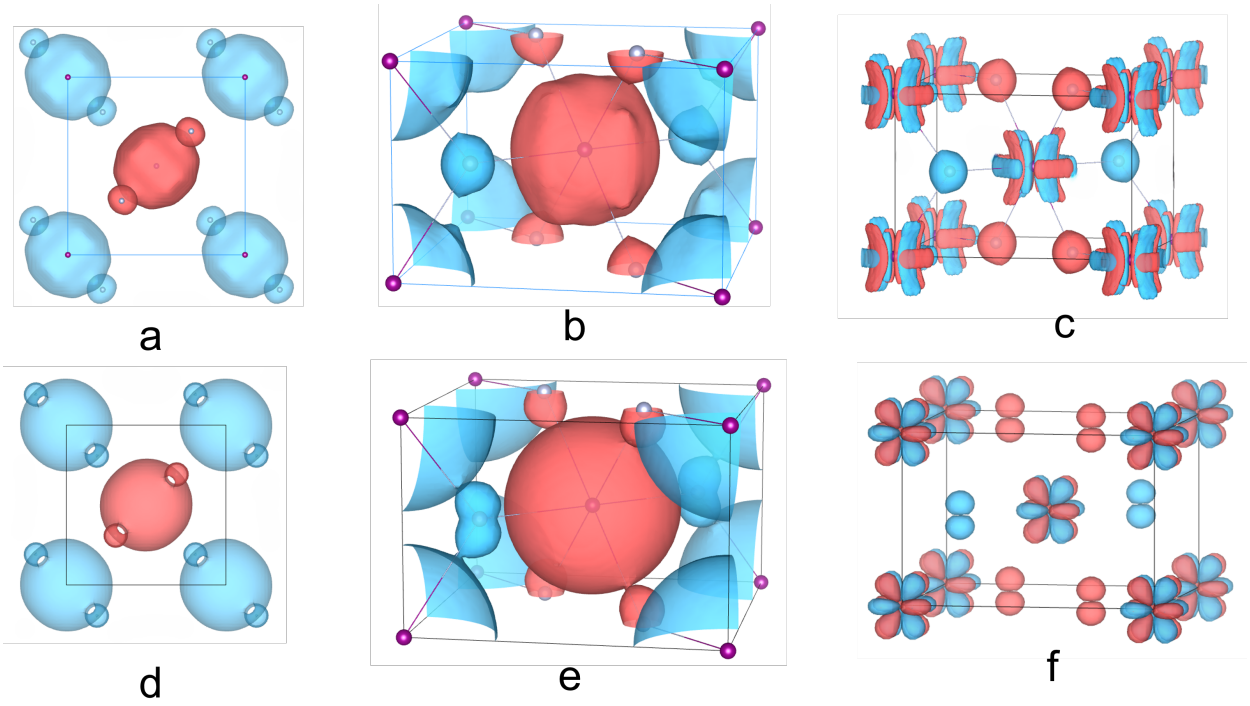

FIG. 2. Spin density reconstructed by MEM projected on the basal plane (a) and in three dimensions (b) at 2 K and 1 T. Spin density deformation map of the 1 T dataset obtained by subtraction of Mn spherical contribution, demonstrating the multipolar character of the Mn spin distribution (c). Model spin density obtained by multipole refinement of the 1T dataset projected on the basal plane described in the main text (d) and in three dimensions (e) showing the fluorine density exhibiting a p_z-like character. Model spin density after subtracting the dominant spherical Mn contribution revealing ferroic order of the O_{52} rank-5 magnetic multipole (f). Isosurface level of $0.02\,\mu_B/\text{Å}^3$ is shown in all figures.

fluorine spin density and a slight asphericity of the Mn magnetization.

MEM analysis of the 6 T dataset yields a nearly identical spin-density distribution, apart from the expected overall sign inversion associated with the domain reversal (see [36]). Thus, within experimental precision, the application of a 6 T magnetic field does not produce detectable changes in the magnetization density.

The aspherical component of the Mn moment, μ^a_{Mn}, and the ligand spin density arising from *p-d* hybridization are expected to be small. By subtracting the spherical part of the Mn spin density from the MEM reconstruction, we obtain the deformation density shown in Fig. 2c. The deformation map confirms the unbalanced, opposite spin polarization on the

ligand sites and reveals, rather than a pure octupolar pattern, a more complex multipolar distribution with zero net magnetic moment at the Mn site, yet still compatible with ferroic multipolar ordering.

D. Multipolar Ordering

The magnetic octupoles that constitute the next term in the magnetic multipole expansion beyond the dipolar and magnetoelectric multipoles may be induced by an external magnetic field or arise spontaneously from the internal molecular field in magnetically ordered compounds. In d-wave altermagnets such as MnF_2, they represent the lowest-order ferroically ordered magnetic quantity and serve as the natural order parameter for the transition into the altermagnetic state [20, 21]. Density functional calculations show that the first allowed magnetic multipole in MnF_2 with the altermagnetic symmetries is the ferroic magnetic octupole of O_{32} symmetry, with real-space form $xy\,m_z$ [20].

The presence of such an octupole implies a slight deviation of the Mn magnetization density from spherical symmetry. Because these local deformations respect the magnetic site symmetry, they cancel when averaged over the Mn positions. To quantify the asphericity, we employ a multipole-expansion formalism. We expand the density of an atom ρ_a as a product of a radial function $R_a(r)$ and real spherical harmonics Y_{lm}. Then the magnetisation density at a given point is calculated as a sum of $m_a\rho_a$ over all magnetic atoms in the unit cell

$$\rho_a(\mathbf{r}) = \sum_{l=0}^{4} R_{l,a}^2(r) \sum_{m=-l}^{l} P_{lm,a}\, Y_{lm}\left(\frac{\mathbf{r}}{r}\right), \tag{6}$$

where Y_{lm} are normalized real spherical harmonics. The local coordinate system is chosen with $z \parallel c$ and $x \parallel [100]$. Slater-type radial functions were used for Mn and F. The resulting magnetic form factor,

$$f_a(\mathbf{k}) = \int \rho_a(\mathbf{r})\, e^{i\,\mathbf{k}\cdot\mathbf{r}}\, d\mathbf{r}, \tag{7}$$

is then inserted into the general expression for the neutron cross section given in Eq. 12 in the supplementary section.

To identify the symmetry-allowed magnetic multipoles, we analyzed the Mn site symmetry, (D_{2h}), generated by the operations $C_{2,[001]}, C_{2,[110]}$, and inversion. Up to (l=4), the invariant basis functions are z^2, xy, $35z^4 - 30z^2 + 3$, and $2xy(7z^2 - 1)$, corresponding to the spherical harmonics Y_{20}, $Y_{2,-2}$, Y_{40}, and $Y_{4,-2}$. The $Y_{2,-2}$ and $Y_{4,-2}$ contributions lead,

respectively, to the symmetry-allowed magnetic multipole order parameters $O_{32} \propto xym_z$ and $O_{52} \propto xyz^2m_z$ both of which are constrained to be ferroic by the magneto-crystalline symmetries. In the preceding discussion we have focussed on multipoles with altermagnetic symmetries in m_z but multipoles in other components m_x, m_y are also expected to arise [37]. The experimental results presented here are not sensitive to these noncollinear multipoles that would also be interesting to probe using polarized neutron scattering.

All collinear symmetry-allowed multipoles were refined against the 1 T and 6 T polarized-neutron diffraction data. The results for the 1 T data set are summarized in Table I. A refinement including only the spherical Mn magnetic form factor (Model 1) accurately reproduces the *odd* reflections, confirming that these reflections are insensitive to the aspherical component of the magnetization density. In contrast (see below), the *even* reflections require progressively higher-order multipolar terms, demonstrating that they directly probe the anisotropic spin density associated with ferroic multipolar order.

TABLE I. Multipolar refinement models for the 2 K, 1 T data set using Slater-type radial functions. Agreement factors are given separately for the full odd dataset ($N_{\mathrm{peak}} = 140$) and *observed* even ($N_{\mathrm{peak}} = 57$) reflections.

Model	1	2	3	4
$m_{\mathrm{Mn}}P_{00}$ (μ_B)	−5.17(5)	−5.17(5)	−5.17(5)	−5.18(5)
$m_{\mathrm{F}}P_{00}$ (μ_B)	0.0	0.0278(10)	0.0318(10)	0.0298(12)
$m_{\mathrm{F}}P_{20}$ (μ_B)	0.0	0.0	0.0063(8)	0.0033(5)
$m_{\mathrm{Mn}}P_{2-2}$ (μ_B)	0.0	0.0	0.0135(8)	0.0
$m_{\mathrm{Mn}}P_{4-2}$ (μ_B)	0.0	0.0	0.0	0.0648(23)
χ^2/N_{peak} (odd)	5.85	5.80	5.78	5.79
χ^2/N_{peak} (even)	101.97	9.03	3.42	1.64

Consistently with the initial fits, refinement of the even reflections requires inclusion of the fluorine monopole term, P_{00} (Model 2), demonstrating that a finite magnetic moment on the fluorine atoms is essential for reproducing the observed intensities.

Further improvement in the description of the even reflections is achieved by introducing aspherical magnetization densities. For the magnetic point group, the lowest-order symmetry-allowed basis functions up to $l = 2$ are z^2 and xy, corresponding to the spherical

harmonics Y_{20} and Y_{2-2}, respectively. Including the theoretically predicted Mn P_{2-2} coefficient (Model 3) reduces the discrepancy for the even reflections by nearly a factor of three, while the additional fluorine P_{20} term provides only a modest further improvement.

Motivated by the MEM reconstruction, which exhibits a magnetization-density deformation resembling a hexadecapolar pattern, we also tested the fourth-order harmonics Y_{40}, Y_{4-2}, and Y_{4-4}. Among these, inclusion of the Mn P_{4-2} coefficient (Model 4), associated with the rank-5 magnetic multipole O_{52}, yields the best agreement with experiment, reducing the misfit for the even reflections to $\chi^2/N_{\mathrm{peak}} = 1.64$.

To qualitatively assess the origin of the improved agreement, we estimated the observed and calculated Fourier components of the magnetization density using the approximate relation

$$F_{M,\mathrm{obs(calc)}} \approx \frac{F_N A_{s,\mathrm{obs(calc)}}}{2}, \tag{8}$$

which applies to even reflections with flipping ratios close to unity. For the odd reflections, for which $R \gg 1$, we instead used

$$F_{M,\mathrm{obs(calc)}} \approx F_N A_{s,\mathrm{obs(calc)}}. \tag{9}$$

The observed and calculated magnetic Fourier components for the *odd* reflections are compared in Fig. 3a,c, where the area of each circle is proportional to the magnitude of the corresponding Fourier component. The excellent agreement between experiment and Model 4 confirms that the spherical component of the Mn magnetization density is accurately reproduced. Consistent with the symmetry of the antiferromagnetic structure, the *odd* Fourier components preserve fourfold rotational symmetry.

By contrast, the Fourier components of the *even* reflections (Fig. 3b,d), which probe the aspherical component of the magnetization density, change sign under a (90°) rotation. This alternating sign pattern is the reciprocal-space fingerprint of altermagnetism. Model 4 quantitatively reproduces both the amplitudes and the sign reversal observed experimentally, providing direct evidence for the anisotropic spin density associated with the ferroic multipolar order.

The respective roles of the ligand and multipolar contributions are illustrated in Fig. 4, where the Fourier components arising from the fluorine magnetic moment and the Mn P_{4-2} multipole are shown separately. The fluorine contribution accounts remarkably well for the low-index reflections but rapidly decreases with increasing scattering vector and therefore

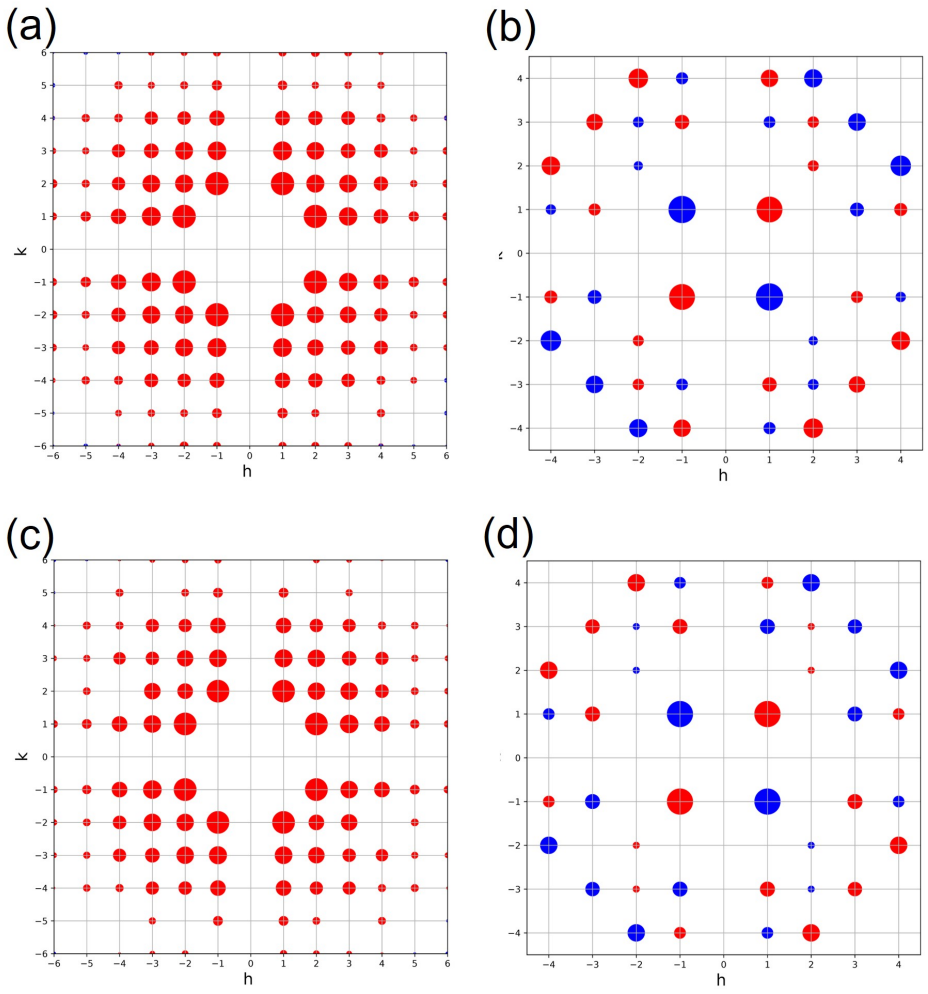

FIG. 3. Fourier components of the magnetization density. (a,b) Experimental Fourier components derived from the 1 T polarized-neutron diffraction data for the *odd* (a) and *even* (b) reflections. (c,d) Corresponding Fourier components calculated using Model 4 for the *odd* (c) and *even* (d) reflections. The area of each circle is proportional to the magnitude of the corresponding Fourier component. Blue and red circles denote positive and negative Fourier components, respectively. Circle size scale factor 40 is applied to the *even* Fourier components for visibility.

cannot reproduce the high-index reflections. This behavior reflects the rapid decay of the ligand p-orbital radial function, further enhanced by Mn–F hybridization. In contrast, the Mn P_{4-2} multipole contributes only weakly at low q but becomes the dominant anisotropic contribution at large scattering vectors, where it is essential for reproducing the observed intensities.

We also tested the other symmetry-allowed $m = 0$ multipoles (P_{20} and P_{40}), but their

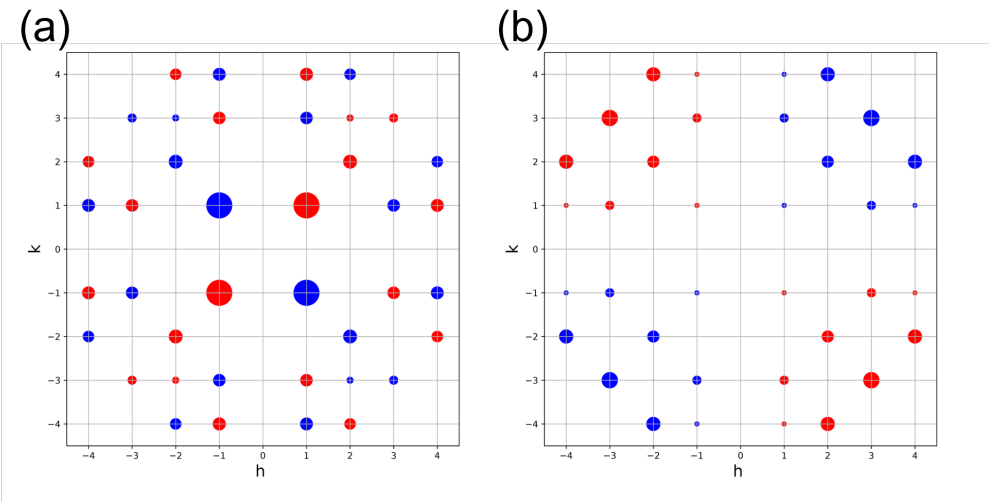

FIG. 4. Fourier components of calculated magnetization density (Model 4) of the even hkl from 1 T dataset projected onto the (001) plane. (a) Fluorine $m_{\mathrm{F}}(P_{00} + P_{20})$ and (b) manganese $m_{\mathrm{Mn}}P_{4-2}$ components of the density respectively.

inclusion did not improve the refinement, effectively ruling out significant contributions from $m = 0$ magnetic multipoles.

The resulting spin-density distribution (Model 4) is shown in Fig. 2d,e. Subtracting from the refined model of the spin density the dominant spherical Mn term of $-5.17(4)\,\mu_B$ isolates the deformation spin density shown in Fig. 2f. The maps reveal ferroic order of the O_{52} rank-5 magnetic multipole (or magnetic triacontadipole) and an imbalance of spin density on the fluorine sites, reflecting time-reversal symmetry breaking of the four-fold screw axis. A close correspondence between this model density and the deformation map obtained from the MEM reconstruction is clearly visible. The fluorine density exhibits a p_z-like character, although this feature should be interpreted cautiously given the small magnitude of P_{20}^{F}.

While the contribution of the P_{2-2} multipole cannot be totally excluded, beyond the improvement in the fit and the indications from the MEM reconstruction, the advantage of the P_{4-2} model is also reflected in the orientation of its density lobes. In the P_{4-2} case, the lobes point toward the strongest fluorine bonds (Fig. 5), whereas in the P_{2-2} model they lie in the basal plane, where the basal plane exchange pathway including two fluorine ions is comparatively weak. Experimentally distinguishing between the P_{2-2} and P_{4-2} Mn multipoles would require measurements of reflections with indices $l > 1$, which were unfortunately not accessible on the D3 diffractometer.

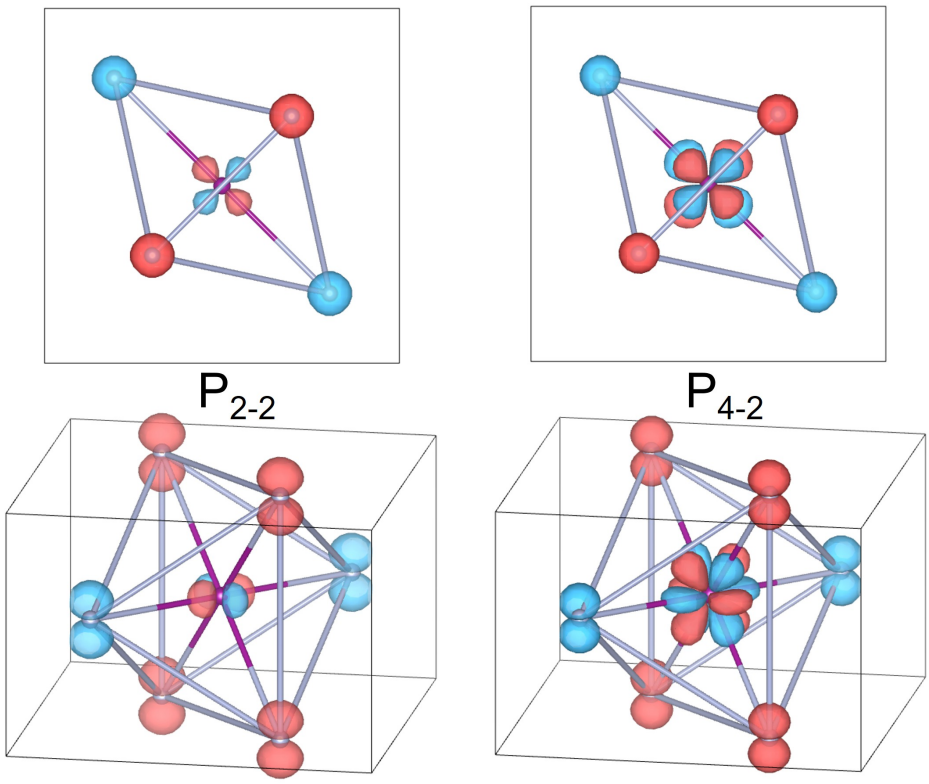

FIG. 5. Spin density distribution within the fluorine cluster combined with $P_{2-2,\mathrm{Mn}}$ and $P_{4-2,\mathrm{Mn}}$ multipoles from models 3 and 4, respectively after subtracting the dominant spherical Mn contribution. Top and bottom figures represent projection onto the ab plane and three dimensional spin density distribution, respectively. The isosurface level of $0.02\,\mu_B/\mathrm{\AA}^3$ is shown.

A similar refinement performed for the 6 T dataset, has shown that within experimental uncertainty, the multipolar decomposition remains essentially unchanged (SI).

Thus, both refinements provide clear evidence for multipoles on the manganese sites incorporating the altermagnetic symmetries. The small but robust fluorine spin density, antiparallel to the nearest neighbor (nn) Mn moment, is likewise confirmed. The absence of significant field-induced changes up to 6 T indicates that the ferro-octupolar order is governed primarily by the Mn molecular field.

IV. CONCLUSION

Polarized-neutron diffraction provides direct real-space evidence of altermagnetic order in MnF_2. The measurements reveal a robust covalent spin polarization on the fluorine ligands, ($\mu_F = 0.029(1), \mu_B$), antiparallel to the nearest-neighbor Mn moments, and a Mn magnetization density that cannot be described by a purely spherical magnetic form factor. Maximum-entropy reconstructions and symmetry-constrained multipole refinements consistently identify the leading magnetic multipoles permitted by the (D_{2h}) site symmetry, including the triacontadipolar component (O_{52}^-). The absence of measurable changes in the spin density up to 6 T indicates that the ferroic multipolar order is dominated by the internal exchange field rather than by the applied magnetic field. More broadly, our work demonstrates that polarized-neutron diffraction can directly resolve the microscopic real-space signatures of altermagnetism, providing a powerful approach for identifying and quantifying ferroic multipoles in altermagnetic materials.

Acknowledgements – We acknowledge financial support from the Fédération Française de Diffusion Neutronique (2FDN). PM acknowledges funding from the CNRS and Springboard grant (ANR-21-EXE5-0003).

[1] M. Naka, S. Hayami, H. Kusunose, Y. Yanagi, Y. Motome, and H. Seo, Spin current generation in organic antiferromagnets, Nature Communications **10**, 4305 (2019), arXiv:1902.02506 [cond-mat.str-el].

[2] L. Šmejkal, R. González-Hernández, T. Jungwirth, and J. Sinova, Crystal time-reversal symmetry breaking and spontaneous Hall effect in collinear antiferromagnets, Science Advances **6**, eaaz8809 (2020).

[3] S. Hayami, Y. Yanagi, and H. Kusunose, Momentum-Dependent Spin Splitting by Collinear Antiferromagnetic Ordering, Journal of the Physical Society of Japan **88**, 123702 (2019), arXiv:1908.08680 [cond-mat.str-el].

[4] L.-D. Yuan, Z. Wang, J.-W. Luo, E. I. Rashba, and A. Zunger, Giant momentum-dependent spin splitting in centrosymmetric low-z antiferromagnets, Phys. Rev. B **102**, 014422 (2020).

[5] L. Šmejkal, A. Marmodoro, K.-H. Ahn, R. González-Hernández, I. Turek, S. Mankovsky, H. Ebert, S. W. D'Souza, O. Šipr, J. Sinova, and T. Jungwirth, Chiral magnons in altermagnetic RuO_2, Phys. Rev. Lett. **131**, 256703 (2023).

[6] L. Šmejkal, J. Sinova, and T. Jungwirth, Emerging Research Landscape of Altermagnetism, Phys. Rev. X **12**, 040501 (2022).

[7] T. Jungwirth, J. Sinova, R. M. Fernandes, Q. Liu, H. Watanabe, S. Murakami, S. Nakatsuji, and L. Smejkal, Symmetry, microscopy and spectroscopy signatures of altermagnetism, arXiv e-prints , arXiv:2506.22860 (2025), arXiv:2506.22860 [cond-mat.mtrl-sci].

[8] R. D. Gonzalez Betancourt, J. Zubáč, R. Gonzalez-Hernandez, K. Geishendorf, Z. ŠobáÅ, G. Springholz, K. Olejník, L. Šmejkal, J. Sinova, T. Jungwirth, S. T. B. Goennenwein, A. Thomas, H. Reichlová, J. Železný, and D. Kriegner, Spontaneous Anomalous Hall Effect Arising from an Unconventional Compensated Magnetic Phase in a Semiconductor, Phys. Rev. Lett. **130**, 036702 (2023), arXiv:2112.06805 [cond-mat.mtrl-sci].

[9] S. Lee, S. Lee, S. Jung, J. Jung, D. Kim, Y. Lee, B. Seok, J. Kim, B. G. Park, L. Šmejkal, C.-J. Kang, and C. Kim, Broken Kramers Degeneracy in Altermagnetic MnTe, Phys. Rev. Lett. **132**, 036702 (2024).

[10] Z. Liu, M. Ozeki, S. Asai, S. Itoh, and T. Masuda, Chiral Split Magnon in Altermagnetic MnTe, Phys. Rev. Lett. **133**, 156702 (2024).

[11] T. Osumi, S. Souma, T. Aoyama, K. Yamauchi, A. Honma, K. Nakayama, T. Takahashi, K. Ohgushi, and T. Sato, Observation of a giant band splitting in altermagnetic mnte, Phys. Rev. B **109**, 115102 (2024).

[12] M. Hajlaoui, S. Wilfred D'Souza, L. Šmejkal, D. Kriegner, G. Krizman, T. Zakusylo, N. Olszowska, O. Caha, J. Michalička, J. Sánchez-Barriga, A. Marmodoro, K. Výborný, A. Ernst, M. Cinchetti, J. Minar, T. Jungwirth, and G. Springholz, Temperature Dependence of Relativistic Valence Band Splitting Induced by an Altermagnetic Phase Transition, Advanced Materials **36**, 2314076 (2024), arXiv:2401.09187 [cond-mat.mtrl-sci].

[13] S. Reimers, L. Odenbreit, L. Šmejkal, V. N. Strocov, P. Constantinou, A. B. Hellenes, R. Jaeschke Ubiergo, W. H. Campos, V. K. Bharadwaj, A. Chakraborty, T. Denneulin, W. Shi, R. E. Dunin-Borkowski, S. Das, M. Kläui, J. Sinova, and M. Jourdan, Direct observation of altermagnetic band splitting in CrSb thin films, Nature Communications **15**, 2116 (2024), arXiv:2310.17280.

[14] M. Zeng, M.-Y. Zhu, Y.-P. Zhu, X.-R. Liu, X.-M. Ma, Y.-J. Hao, P. Liu, G. Qu, Y. Yang, Z. Jiang, K. Yamagami, M. Arita, X. Zhang, T.-H. Shao, Y. Dai, K. Shimada, Z. Liu, M. Ye, Y. Huang, Q. Liu, and C. Liu, Observation of spin splitting in room-temperature metallic antiferromagnet crsb, Advanced Science **11**, 2406529 (2024), https://arxiv.org/abs/2405.12679.

[15] G. Yang, Z. Li, S. Yang, J. Li, H. Zheng, W. Zhu, Z. Pan, Y. Xu, S. Cao, W. Zhao, A. Jana, J. Zhang, M. Ye, Y. Song, L.-H. Hu, L. Yang, J. Fujii, I. Vobornik, M. Shi, H. Yuan, Y. Zhang, Y. Xu, and Y. Liu, Three-dimensional mapping of the altermagnetic spin splitting in CrSb, Nature Communications **16**, 1442 (2025), arXiv:2405.12575.

[16] J. Ding, Z. Jiang, X. Chen, Z. Tao, Z. Liu, T. Li, J. Liu, J. Sun, J. Cheng, J. Liu, Y. Yang, R. Zhang, L. Deng, W. Jing, Y. Huang, Y. Shi, M. Ye, S. Qiao, Y. Wang, Y. Guo, D. Feng, and D. Shen, Large band splitting in g-wave altermagnet crsb, Phys. Rev. Lett. **133**, 206401 (2024).

[17] W. Lu, S. Feng, Y. Wang, D. Chen, Z. Lin, X. Liang, S. Liu, W. Feng, K. Yamagami, J. Liu, C. Felser, Q. Wu, and J. Ma, Signature of Topological Surface Bands in Altermagnetic Weyl Semimetal CrSb, Nano Letters **25**, 7343 (2025), arXiv:2407.13497 [cond-mat.mtrl-sci].

[18] Q. Faure, D. Bounoua, V. Balédent, A. Gukasov, V. Ovidiu Garlea, A. Ribeiro, J. G. Rau, S. Petit, and P. McClarty, Altermagnetism revealed by polarized neutrons in MnF_2, arXiv e-prints , arXiv:2509.07087 (2025), arXiv:2509.07087 [cond-mat.str-el].

[19] S. Hayami, Y. Yanagi, and H. Kusunose, Bottom-up design of spin-split and reshaped electronic band structures in antiferromagnets without spin-orbit coupling: Procedure on the basis of augmented multipoles, Phys. Rev. B **102**, 144441 (2020).

[20] S. Bhowal and N. A. Spaldin, Ferroically ordered magnetic octupoles in d-wave altermagnets, Phys. Rev. X **14**, 011019 (2024).

[21] P. A. McClarty and J. G. Rau, Landau theory of altermagnetism, Phys. Rev. Lett. **132**, 176702 (2024).

[22] H. Schiff, P. McClarty, J. G. Rau, and J. Romhányi, Collinear altermagnets and their landau theories, Phys. Rev. Res. **7**, 033301 (2025).

[23] X. H. Verbeek, D. Voderholzer, S. Schären, Y. Gachnang, N. A. Spaldin, and S. Bhowal, Nonrelativistic ferromagnetotriakontadipolar order and spin splitting in hematite, Phys. Rev. Res. **6**, 043157 (2024).

[24] M. M. R. Costa and P. J. Brown, Magnetisation density in MnF $_2$, Physica B Condensed Matter **156**, 329 (1989).

[25] R. Nathans, H. Alperin, S. Pickart, and P. Brown, Measurement of the covalent spin distribution in manganous fluoride using polarized neutrons, Journal of Applied Physics **34**, 1182 (1963).

[26] I. Kibalin and A. Gukasov, Cryspy. crystallographic python library, `https://www.cryspy.fr/`.

[27] J. Jeong, B. Lenz, A. Gukasov, X. Fabrèges, A. Sazonov, V. Hutanu, A. Louat, D. Bounoua, C. Martins, S. Biermann, V. Brouet, Y. Sidis, and P. Bourges, Magnetization density distribution of sr_2iro_4: Deviation from a local $j_{\text{eff}} = 1/2$ picture, Phys. Rev. Lett. **125**, 097202 (2020).

[28] H. A. Alperin, P. J. Brown, R. Nathans, and S. J. Pickart, Polarized neutron study of antiferromagnetic domains in MnF_2, Phys. Rev. Lett. **8**, 237 (1962).

[29] P. A. McClarty, A. Gukasov, and J. G. Rau, Observing altermagnetism using polarized neutrons, Phys. Rev. B **111**, L060405 (2025).

[30] G. P. Felcher and R. Kleb, Antiferromagnetic domains and the spin-flop transition of MnF_2, EPL (Europhysics Letters) **36**, 455 (1996).

[31] J. B. J. Matthewman, Ccsl, ral93-009 (1993).

[32] M.-T. Suzuki, T. Koretsune, M. Ochi, and R. Arita, Cluster multipole theory for anomalous hall effect in antiferromagnets, Phys. Rev. B **95**, 094406 (2017).

[33] S. Hayami and H. Kusunose, Unified Description of Electronic Orderings and Cross Correlations by Complete Multipole Representation, Journal of the Physical Society of Japan **93**, 072001 (2024), arXiv:2403.09019 [cond-mat.str-el].

[34] R. J. Papoular and B. Gillon, Maximum entropy reconstruction of spin density maps in crystals from polarized neutron diffraction data, EPL (Europhysics Letters) **13**, 429 (1990).

[35] J. Karmeshu, *Entropy Measures, Maximum Entropy Principle and Emerging Applications* (Springer-Verlag, 2003).

[36] I. Kibalin, D. Bounoua, J. A. R. Velamazán, O. Fabelo, N. Qureshi, Q. Faure, P. Bourges, V. Balédent, J.-R. Soh, J. Rau, P. McClarty, and A. Gukasov, Supplemental material (url-will-be-inserted-by-publisher).

[37] L. Buiarelli, R. M. Fernandes, and T. Birol, Noncollinear magnetic multipoles in collinear altermagnets, Phys. Rev. B **112**, 224442 (2025).

[38] P. J. Becker and P. Coppens, Extinction within the limit of validity of the Darwin transfer equations. I. General formalism for primary and secondary extinction and their applications to spherical crystals, Acta Crystallographica Section A **30**, 129 (1974).

[39] A. Delapalme, G. H. Lander, and P. J. Brown, Magnetisation density in URh_3, Journal of Physics C: Solid State Physics **11**, 1441 (1978).

SUPPLEMENTARY INFORMATION

Polarized Neutron Cross Section

The scattering intensity for polarized neutrons in the elastic channel is given by

$$I^{\pm}(\mathbf{k}) \propto |N(\mathbf{k})|^2 + |\mathbf{M}_{\perp}(\mathbf{k})|^2 \;\pm\; 2\,\Re\Big[N(\mathbf{k})\,\mathbf{P}_0 \cdot \mathbf{M}_{\perp}^{*}(\mathbf{k})\Big], \tag{10}$$

where the nuclear structure factor is

$$N(\mathbf{k}) = \sum_j b_j\, e^{i\mathbf{k}\cdot\mathbf{r}_j}, \tag{11}$$

and the magnetic interaction vector is

$$\mathbf{M}_{\perp}(\mathbf{k}) = \sum_j \frac{r_0\gamma}{2}\, f_j(\mathbf{k})\, e^{i\mathbf{k}\cdot\mathbf{r}_j} \Big[\hat{\mathbf{k}} \times \big(\mathbf{m}_j \times \hat{\mathbf{k}}\big)\Big]. \tag{12}$$

Here $\hat{\mathbf{k}} = \mathbf{k}/|\mathbf{k}|$, $f_j(\mathbf{k})$ is the magnetic form factor, and $\mathbf{m}_j$ is the magnetic moment of atom j. This general expression allows refinement of the magnetic structure using either spherical or multipolar form factors, provided that nuclear and magnetic scattering occur at the same reciprocal-lattice positions, as is the case for MnF_2. In Eq. 10 we have omitted the polarization dependent chiral term because it vanishes in MnF_2 in the elastic channel as a consequence of the reality of $\mathbf{M}_{\perp}(\mathbf{k})$ which, in turn, comes from the existence of an inversion center.

Data Refinement

Prior to the polarized-neutron measurements, the nuclear and magnetic structures were characterized on the four-circle diffractometer D9 at the Institut Laue–Langevin (ILL) using neutrons of wavelength $\lambda = 0.82$ Å. MnF_2 crystallizes in the tetragonal space group $P4_2/mnm$ with lattice parameters $a = b = 4.87$ Å and $c = 3.30$ Å. The Mn ions occupy the $2a$ sites and the fluorine ions the $4f$ sites. The refined structural parameters, $x_{\mathrm{F}} = 0.3049(2)$, $B_{\mathrm{iso,F}} = 0.388(16)$, $B_{\mathrm{iso,Mn}} = 0.155(35)$, and $\mathrm{Occ_F} = 0.992(5)$, were used in the subsequent polarized-neutron analysis.

Polarized-neutron diffraction refinements for the 2 K, 1 T data set were based on the measured flipping ratios. The odd reflections, dominated by the spherical part of the Mn

form factor, exhibit extremely large variations in flipping ratio, ranging from $0.02 < R < 50$. To stabilize the refinement, we used the asymmetry parameter

$$\mathrm{As} = \frac{R-1}{R+1},$$

which balances the weight of reflections with $R > 1$ and $R < 1$ in the agreement factor. With an exposure time of 5 minutes per reflection, about 70% of the measured asymmetries exceeded the 3σ threshold for As(hkl).

In contrast, the flipping ratios of even reflections—sensitive to fluorine covalence and Mn asphericity—differed from unity by only a few percent. For this reason, an exposure time of 30 minutes per reflection was required. Because a complex spin-density distribution was anticipated, all symmetry-allowed even reflections in four unique sets were measured up to $\sin\theta/\lambda < 0.8$ Å^{-1}. This yielded a 1 T data set consisting of 140 reflections, of which 57 exceeded the 2σ threshold for As(hkl). The multipolar refinements were performed using the full odd-reflection data set and a threshold-filtered subset of even reflections selected for their high sensitivity to variations in the model parameters. The resulting parameters for 1 T data set are reported in the main text.

TABLE II. Multipolar refinement models for the 2 K, 6 T data set using Slater-type radial functions. Agreement factors are given separately for *all odd* ($N_{\mathrm{peak}} = 47$) and *observed even* reflections ($N_{\mathrm{peak}} = 32$).

Model	1	2	3	4
$m_{\mathrm{Mn}}P_{00}$ (μ_B)	5.17(5)	5.17(5)	5.17(5)	5.17(5)
$m_{\mathrm{F}}P_{00}$ (μ_B)	0.0	−0.0275(10)	−0.0301(10)	−0.0277(12)
$m_{\mathrm{F}}P_{20}$ (μ_B)	0.0	0.0	−0.0064(8)	−0.0028(5)
$m_{\mathrm{Mn}}P_{2-2}$ (μ_B)	0.0	0.0	−0.0167(20)	0.0
$m_{\mathrm{Mn}}P_{4-2}$ (μ_B)	0.0	0.0	0.0	−0.082(8)
χ^2/N_{peak} (odd)	5.14	5.14	5.14	5.14
χ^2/N_{peak} (even)	56.45	5.90	4.81	3.45

Refinement of the 6 T data set (Table II), comprising 47 odd and 83 even reflections measured with a 20-minute exposure time, yielded 32 observed even reflections. As for the

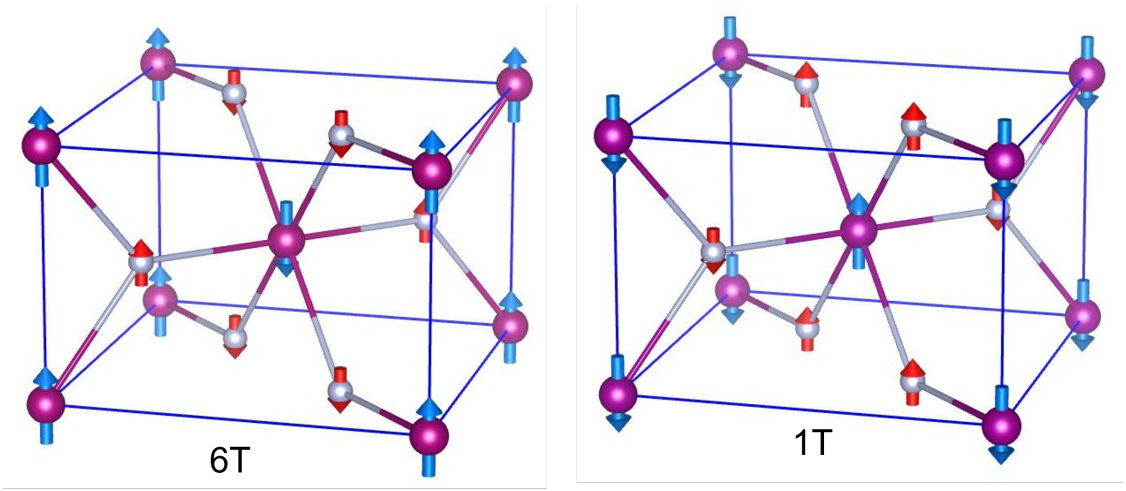

FIG. 6. Left: magnetic domain $\mathbf{N}_-$; right: $\mathbf{N}_+$ in MnF_2 at 2 K, 1 T and 6 T. Red arrows show Mn moments; blue arrows show fluorine moments (scaled by 10^2 for visibility).

1 T data set, the odd reflections are fully described by the spherical Mn magnetic form factor, whereas the even reflections require both a finite ligand spin density and an anisotropic Mn magnetization density. The best agreement is again obtained with Model 4, confirming the presence of the Mn P_{4-2} multipole together with an antiparallel spin polarization on the fluorine ions. As expected upon reversal of the magnetic field, all refined magnetic coefficients change sign while retaining essentially the same magnitudes within the experimental uncertainties.

A refinement of the 6 T data set, with the domain population allowed to vary, shows that following the spin-flop transition, the N_+ domain occupies 88(1)% of the sample volume. The reversal of the Néel vector upon the spin-flop transition reverses the signs of the Mn and F moments, while their magnitudes remain unchanged within the experimental uncertainties. This indicates that the application of a 6 T field has only a minor effect on the magnetic structure.

The corresponding magnetic structures of the refined majority domains, obtained using spherical Model 2 for the 1 T and 6 T data sets, are shown in Fig. 6.

Within the experimental precision, no significant field-induced changes in either the ligand polarization or the Mn multipolar coefficients are observed between 1 and 6 T. This robustness indicates that the ferro-octupolar order is governed primarily by the internal Mn molecular field rather than by the externally applied magnetic field.

Multipolar Modulation of Exchange Interactions

The refined spin density shows that the Mn magnetization is not purely spherical but contains a small tesseral hexadecapole P_{4-2}. This multipole transforms as $(x^2 - y^2)(7z^2 - r^2)$ in the $(x, y, z) \parallel ([110], [1\bar{1}0], [001])$ frame and introduces a four-lobed anisotropy that distinguishes the $3d_{xz}$ and $3d_{yz}$ orbitals. This anisotropy directly affects the Mn–F–Mn superexchange pathways.

For the nearest-neighbour ferromagnetic path J_1 (bond angle 101.27°), both Mn ions contribute mainly $3d_{xz}$ orbitals. The P_4^{-2} multipole enhances the spin density along x, increasing the $3d_{xz}$–$2p_z$–$3d_{xz}$ overlap and strengthening the ferromagnetic exchange.

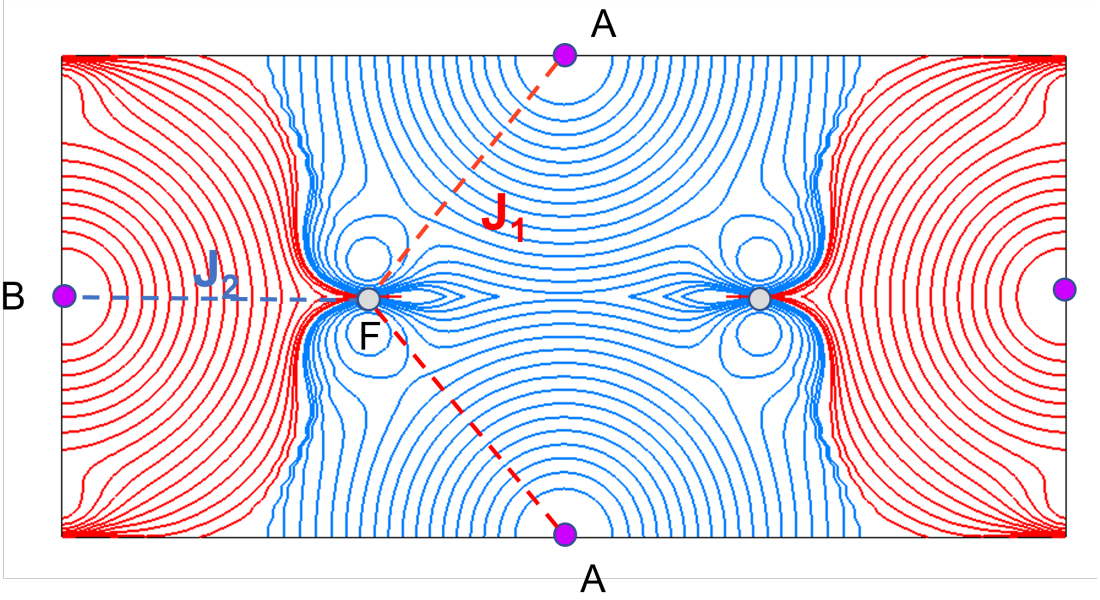

FIG. 7. Spin density in the (110) plane centered at the $(\frac{1}{2}, \frac{1}{2}, \frac{1}{2})$ position, showing the ferromagnetic and antiferromagnetic exchange paths J_1 and J_2 mediated by the fluorine p_z orbitals.

The next-nearest-neighbour (nnn) path J_2 (129.4°) involves mixed $3d_{xz}$ and $3d_{yz}$ orbitals results in the antiferromagnetic character of J_2 in agreement with Goodenough-Kanamori rules.

The most significant effect occurs for the 180° double-ligand path J_7 in the basal plane. This path couples $3d_{xz}$ orbitals on opposite sublattices through two fluorine $2p_z$ orbitals. Since P_4^{-2} is maximal in the basal plane and changes sign under the $4_2'$ symmetry operation, it induces alternating exchange anisotropies on the two Mn sublattices. This

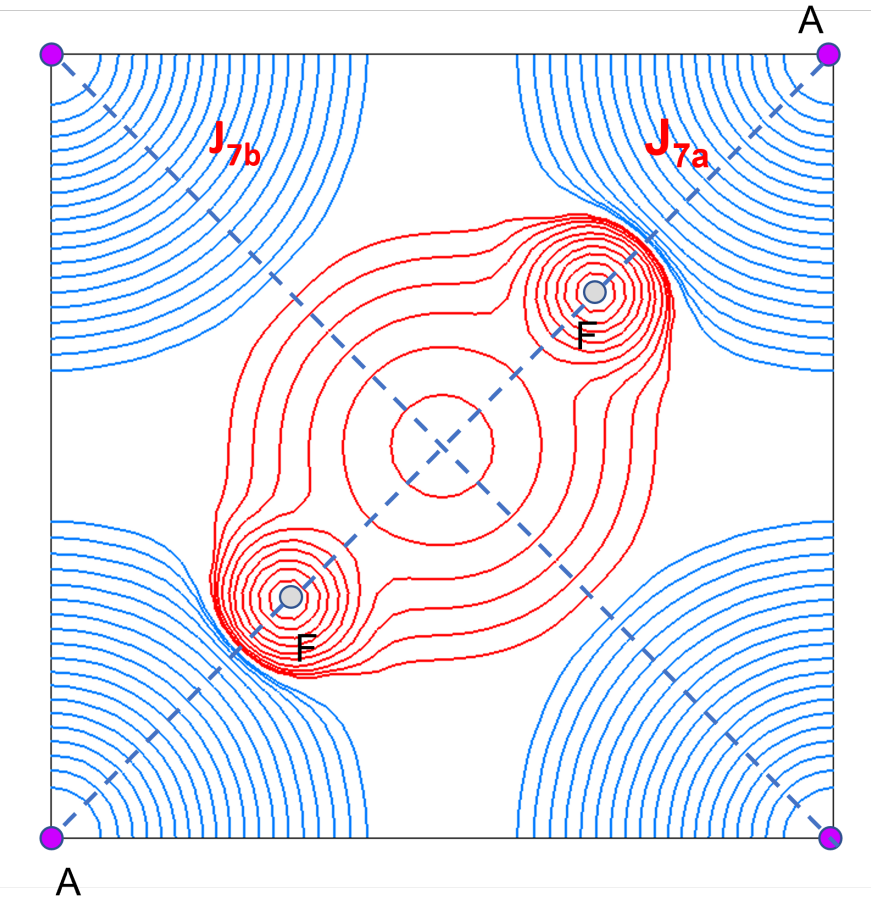

FIG. 8. Spin density in the basal plane showing the ferromagnetic exchange path J_{7a} mediated by hybridization of two fluorine p_z orbitals.

sublattice-dependent modulation provides a natural microscopic mechanism for the emergence of altermagnetic symmetry [5, 18].

Overall, the P_4^{-2} hexadecapole is not a minor correction but an active element shaping the exchange network and reinforcing the altermagnetic topology of MnF_2.

Maximum Entropy Method

To assess the asphericity of the Mn spin density, several MEM reconstructions were performed on the 1 T and 6 T data sets using deliberately unfavorable, non-uniform priors [34]. The prior consists of spherically symmetric magnetization densities centered on the Mn and F sites, constructed analytically from the refined moments and the radial integrals obtained

in the least-squares refinement. Because this prior is strongly biased toward spherical densities, any asphericity emerging in the MEM solution must be supported directly by the experimental data.

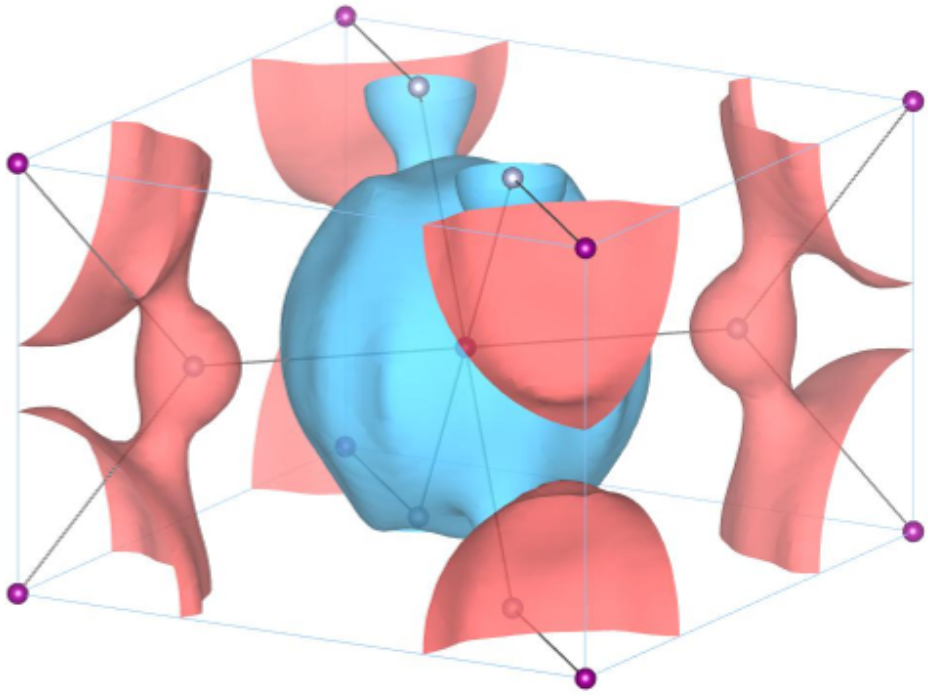

FIG. 9. MEM reconstructed spin density at 2 K in 6 T with isosurface level taken to be $0.02\,\mu_B/\text{Å}^3$.

Figures 9 shows the reconstructed three-dimensional spin density for the 6 T data set at 2 K. The MEM reconstruction of the 6 T data containing less statistically significant reflections yields a spin-density distribution very close to that of the 1 T state, apart from the expected global sign inversion associated with the domain reversal. Thus, within experimental precision, the application of a 6 T magnetic field does not produce significant changes in the magnetization density.

Domain Population Control

Magnetic domain populations were determined prior to each measurement using the polarized–neutron flipping–ratio method of Alperin *et al.* [28]. Bragg intensities for neutron spins parallel (I^+) and antiparallel (I^-) to the applied field yield the flipping ratio

$$R = I^+/I^-.$$

For MnF_2, the nuclear and magnetic structure factors of the (320)-type reflections are nearly equal at low temperature, and the ratio reduces to

$$R = \frac{1 + P_i(2\alpha - 1)}{1 - P_i\epsilon(2\alpha - 1)},$$

where α is the domain fraction and ϵ the spin–flipper efficiency. This expression enables direct extraction of the domain populations from the measured R.

After slow field cooling to 2 K in a 5 T field, flipping ratios of the (3,2,0) and (3,$\bar{2}$,0) reflections were recorded:

At 1 T, the expected relation

$$R_{hkl} = 1/R_{h\bar{k}l}$$

was satisfied, confirming a nearly single antiferromagnetic domain with Néel vector

$$\mathbf{N}_- = -\mathbf{M}_1(0,0,0),\ \mathbf{M}_2\left(\tfrac{1}{2},\tfrac{1}{2},\tfrac{1}{2}\right),$$

opposite to the vertical field direction.

MnF_2 undergoes a spin–flop transition at $\mu_0 H_{\mathrm{sf}} \approx 9.3$ T at 2 K. Due to a slight misalignment of the c axis, the transition occurred at 7.6 T in our experiment. Reducing the field to 6 T restored the antiferromagnetic state but with reversed domain populations: refinement shows that the majority domain with Néel vector

$$\mathbf{N}_+ = \mathbf{M}_1(0,0,0),\ -\mathbf{M}_2\left(\tfrac{1}{2},\tfrac{1}{2},\tfrac{1}{2}\right)$$

occupies $\sim 88\%$ of the sample, while $\sim 12\%$ remains in the original domain. The 6 T data set was collected under these conditions.

TABLE III. Measured flipping ratios and extracted domain fractions.

Reflection	2 K, 1 T	2 K, 6 T
$R_{(3,2,0)}$	0.024(4)	22(2)
$C_{\mathrm{Dom\,1}}$	$\approx 0\%$	$\approx 88\%$
$R_{(3,\bar{2},0)}$	44(4)	0.042(3)
$C_{\mathrm{Dom\,2}}$	$\approx 100\%$	$\approx 12\%$

Extinction Corrections

In the flipping ratio method, the extinction factors y_+ and y_- applied to I_+ and I_-, respectively are usually obtained from an extinction model (e.g. Becker-Coppens [38]) adapted to polarized neutrons. Such an approach is used in CRYSPY [26].

An extinction correction applied to the polarized neutron diffraction has been considered by Delapalme et al. Ref. [39]. They show that those flipping ratios close to unity are much less sensitive to the extinction as, if one assumes $y_+ \approx y_-$, the extinction correction cancels in the flipping ratio. This is the case of *even* reflections yielding flipping ratio close to 1. Therefore in practice, we found that the extinction plays a negligible role in the refinement and reconstruction of spin density from the *even* data sets, which are related to the asphericity and covalency.

We found that the extinction correction applied to the measured even datasets did not exceed a few percent in the refined parameters. However, since the odd reflections, exhibiting strongly different y_+ and y_-, were sensitive to the extinction corrections the Becker–Coppens extinction parameters were applied both to *odd* and *even* datasets. These parameters were obtained by refinement of unpolarized neutron diffraction from D9 diffractometer diffractometer adapted to polarized neutrons.